

Aliovalent cation substitution in UO₂: Electronic and local structures of U_{1-y}La_yO_{2±x} solid solutions

Prieur, D.; Martel, L.; Vigier, J.-F.; Scheinost, A. C.; Kvashnina, K. O.; Somers, J.;
Martin, P. M.;

Originally published:

February 2018

Inorganic Chemistry 57(2018)3, 1535-1544

DOI: <https://doi.org/10.1021/acs.inorgchem.7b02839>

Perma-Link to Publication Repository of HZDR:

<https://www.hzdr.de/publications/Publ-26181>

Release of the secondary publication
on the basis of the German Copyright Law § 38 Section 4.

Aliovalent cation substitution in UO_2 : Electronic and local structures of $\text{U}_{1-y}\text{La}_y\text{O}_{2\pm x}$ solid solutions

D. Prieur^{1,2,3*}, L. Martel¹, J-F. Vigier¹, A.C. Scheinost^{2,3}, K. O. Kvashnina^{2,3}, J. Somers¹, P. M. Martin⁴

¹ European Commission, Joint Research Centre (JRC), Postfach 2340, 76125 Karlsruhe, Germany. ² Helmholtz-Zentrum Dresden-Rossendorf, Institute of Resource Ecology, P.O. Box 10119, 01314 Dresden, Germany. ³ Rossendorf beamline (BM20-CRG), European Synchrotron Radiation Facility, 6 rue Jules Horowitz, BP 220, 38043 Grenoble, France. ⁴ CEA, Nuclear Energy Division, Research Department on Mining and Fuel Recycling Processes, SFMA, BP 17171, F-30207 Bagnols-sur-Cèze, France.

KEYWORDS: UO_2 , Lanthanum, XANES, EXAFS, NMS

ABSTRACT: For nuclear fuel related applications, the oxygen stoichiometry of mixed oxides $\text{U}_{1-y}\text{M}_y\text{O}_{2\pm x}$ is an essential property as it affects the fuel properties and may endanger the safe operation of nuclear reactors. A careful review of the open literature indicates that this parameter is difficult to assess properly and that the nature of the defects, i.e. oxygen vacancies or U^{V} , in aliovalent cation – doped UO_2 is still subject to controversy. To confirm the formation of U^{V} , we have investigated the room temperature stable $\text{U}_{1-y}\text{La}_y\text{O}_{2\pm x}$ phase using several experimental methods (e.g. XRD, XANES and NMR) confirmed by theoretical calculations. This paper presents the experimental proof of U^{V} and its effect we identified in both electronic and local structure. We observe that U^{V} is formed in quasi equimolar proportion as La^{III} in $\text{U}_{1-y}\text{La}_y\text{O}_{2\pm x}$ ($y=0.06; 0.11; 0.22$) solid solutions. The fluorite structure is maintained despite the cationic substitution but the local structure is affected as variations of the interatomic distances are found. Therefore, we provide here the definitive proof that the substitution of U^{IV} with La^{III} is not accommodated by the creation of O vacancies as has often been assumed. The UO_2 fluorite structure compensates the incorporation of an aliovalent cation by the formation of U^{V} in quasi equimolar proportions.

1. INTRODUCTION

The substitution of uranium in UO_2 by aliovalent atoms, like most of the lanthanides and some of the actinides, can lead under specific conditions to the formation of $\text{U}_{1-y}\text{M}_y\text{O}_{2\pm x}$ solid solutions. These materials are encountered in the nuclear field as fuel or transmutation targets but can be also be formed during irradiation for example by the accommodation of fission products (FPs) into the UO_2 structure. The substitution of U by another cation, of lower valence, implies either the formation of oxygen vacancies or of an increase of the U oxidation state. Both charge compensating mechanisms modify the overall oxygen to metal ratio (O/M), with ultimate effects on phase stability, defect chemistry and oxygen chemical potential of the material¹⁻⁵. The O/M ratio is a strong driver of nuclear fuel properties and ultimately of reactor performance and safety. An accurate determination of the oxygen stoichiometry of mixed oxides $\text{U}_{1-y}\text{M}_y\text{O}_{2\pm x}$ is hence crucial, along with a detailed understanding of the nature of the charge compensating defects and their effects on the local structure.

Although the open literature indicates that the O/M ratio may be derived using several methods including thermogravimetric analysis (TGA)⁶⁻⁸, X-ray diffraction (XRD)⁹⁻¹¹, and thermodynamical modelling², the discrepancy of the results often encountered indicates that an accurate determination remains difficult. Indeed, TGA would be the natural method to measure the O/M ratio of an oxide but, in the case of a trivalent substituting cation, one can only assume both initial and final O/M values, or rely on a significant change around the 2.0 ratio. In addition, applying this method to actinides is even more challenging as

an accurate control of the atmosphere is required given their sensitivity to oxygen². The O/M has also been investigated by XRD using Vegard's law and has been described as a function of the lattice parameter in some $\text{U}_{1-y}\text{M}_y\text{O}_{2\pm x}$ ⁹⁻¹¹ compounds. However, for a trivalent M cation, a limitation rises from the hexagonal nature of the sesquioxide M_2O_3 end-members taken into account in the Vegard's law. Regarding the thermodynamical modelling, such calculations of ternary systems are challenging and still under development.

In this context, the purpose of this work is to combine two short-range order spectroscopies, i.e. XAS and NMR, to investigate the electronic and local environments of the U, M and O elements in $\text{U}_{1-y}\text{M}_y\text{O}_{2\pm x}$ solid solutions. X-ray absorption near edge structure (XANES) spectroscopy is an element selective technique providing direct determination of the cation valence states and thus of the O/M ratio of $\text{U}_{1-y}\text{M}_y\text{O}_{2\pm x}$ ^{3,12-15}. In addition, contrary to XRD, extended X-ray absorption fine structure (EXAFS) spectroscopy is sensitive to local environments around one specific target element, which permits a comprehensive investigation on the modification of the local structure induced by the presence of aliovalent cations in UO_2 ^{3,12-15}. Moreover, Nuclear Magnetic Resonance (NMR) of deliberately ¹⁷O enriched materials should be most suitable to complete this picture of the cationic sublattice. The ¹⁷O nucleus is NMR active, therefore providing the O local environment in the oxide 16–18. In view of future studies on $\text{U}_{1-y}\text{AnyO}_{2\pm x}$, this work is focused on a model system $\text{U}_{1-y}\text{La}_y\text{O}_{2\pm x}$ ($y=0.06; 0.11; 0.22$). ¹³⁹La was chosen as doping cation as it is a suitable surrogate for actinides and since it is also NMR active 19. In addition, La

is a fission product formed during nuclear power generation, hence its incorporation into UO₂ is of significant interest.

2. EXPERIMENTAL

2.1 SYNTHESIS

The U_{1-y}La_yO_{2±x} (y=0.06; 0.11; 0.22) samples have been prepared by gel-supported precipitation, also referred as sol-gel external gelation^{13,16}. Uranyl nitrate and ¹³⁹La nitrate solutions were mixed to achieve a molar stoichiometry of $y = \text{La}/(\text{U} + \text{La})$, as defined above. An organic thickener (Methocel, Dow Chemicals) was added to increase the viscosity of the solutions, which were then dropped into an ammonia bath where droplet to particle conversion took place due to hydroxide precipitation of the metals inside the polymer backbone of the droplet. The resulting beads were washed, dried, and then calcined at 873 K in air (2 h) to remove organics and then at 973 K in Ar/H₂ (2 h) to ensure uranium reduction. The samples were then enriched at about 30% in ¹⁷O by heating in ¹⁷O enriched gas at 1073 K (24 h) and then sintered for 4 hours at 1923 K under Ar/H₂.

2.2 CHARACTERIZATION

2.2.1 XRD

The X-ray powder diffraction patterns were obtained at room temperature with ~10 mg of sample using a Bruker D8 Advance diffractometer (40 kV and 40 mA) with a Bragg-Brentano $\theta/2\theta$ configuration and equipped with a Cu K _{α} 1 monochromator and a Lynxeye linear position-sensitive detector. The powder XRD patterns were recorded using a step size of 0.01 and an integration time of 2 s across the angular range $25^\circ \leq 2\theta \leq 120^\circ$. The lattice parameter was refined using the Le Bail method with the powder option of Jana2006 software. Peak profile fitting was done using Pseudo-Voigt functions.

2.2.2 XANES

XAS data acquisition was performed on the oxide powder mixed with BN, the latter being essentially transparent to X-rays in the energy range of interest. XAS data were recorded at the European Synchrotron Radiation Facility (ESRF, France). The storage ring operating conditions were 6.0 GeV and 160-200 mA.

The U L_{III} XAS spectra were recorded at room temperature in transmission mode at the HZDR-operated Rossendorf Beamline (BM20) dedicated to actinide elements²⁰. A double crystal monochromator mounted with a Si (111) crystal was used. The energy calibration was achieved using yttrium (K edge: 17038 eV) foil inserted between the second and third ionization chambers. For each XANES measurement, the spectra of the reference foil were systematically collected at the same time. To determine the oxidation states of U, XANES spectra at L_{III} edges were compared to those of reference samples, i.e. U^{IV}O₂ and (U^{IV}_{0.5}U^V_{0.5})₄O₉^{4,21}, that have been previously collected on the same beamline. Oxidation states for each cation were derived using a linear combination of these normalized reference spectra. The experimental data were fitted between -20 eV and +30 eV with respect to the white line position.

The U M_{IV} and La L_{III} HERFD-XANES (High Energy Resolved Fluorescence Detection) spectra were recorded at the ESRF beamline ID26. The incident energy was selected using the (111) reflection from a double Si crystal monochromator. Rejection of higher harmonics was achieved by three Si mirrors

at an angle of 3.5 mrad relative to the incident beam. XANES spectra were simultaneously measured in total fluorescence yield (TFY) mode using a photodiode and in HERFD mode using an X-ray emission spectrometer²². The sample, analyzer crystals and photon detector (silicon drift detector) were arranged in a vertical Rowland geometry. The HERFD spectra at the U M_{IV} and La L_{III} edges were obtained by recording the intensities of the U M _{β} (~3337 eV) and the La L α ₁ (~4647 eV) emission lines as a function of the incident energy. The emission energy was selected using the (220) reflection of five spherically bent Si crystal analyzers (with 1 m bending radius). The paths of the incident and emitted X-rays through air were minimized in order to avoid losses in intensity due to absorption. To determine the oxidation states of U and La, U_{L_{III}} and La_{L_{III}}XANES spectra edges were compared to those of reference samples that have been previously collected on the same beamline. Spectra of the following reference compounds were used: U^{IV}O₂, (U^{IV}_{0.5}U^V_{0.5})₄O₉ and U^{VI}O₃ and La^{III}₂O₃^{21,23-25}. Oxidation states for each cation were derived using a linear combination of these normalized reference spectra. In the case of U M_{IV} XANES spectra, Iterative Transformation Factor Analysis (ITFA) was used to derive the fractions of U(IV), U(V) and U(VI). This method has already been successfully applied to the EXAFS studies of actinides^{25,26}. IFTA calculates the relative concentrations of components present in each absorption spectrum, considering, as an input, two known distributions of reference systems such as UO₂ (100% of U(IV)) and UO₃ (100% of U(VI)). Note that the method has been fully described by Rossberg *et al.*²⁶.

Lanthanum L3 edge HERFD-XANES spectra of U_{1-y}La_yO_{2±x} spectra were calculated using the Finite Difference Method for Near Edge Structure (FDMNES) code²⁷. Such code allows the calculation of the occupied and unoccupied projected Density Of States (DOS) around an absorption edge. Relativistic effects were taken into account (relativism keyword). The self-consistent calculation of the Fermi level was performed using the SCF keyword. Due to the presence of heavy nucleus (U and La), spin-orbit effects were taken into account in the calculations. Nevertheless, no spin-polarization effect has been noticed. Finally, calculations were performed considering the quadrupole 2p_{3/2}-5f transition probability. The atomic cluster used as input was built by using the Fm-3m structure of the UO₂ using a cluster radius of 6.0 Å around the central La atom leading to a cluster containing 75 atoms. The theoretical spectra were convoluted considering the La 3d_{5/2} core-hole (0.83 eV) and a Gaussian function of 0.5 eV to reproduced experimental broadening.

2.2.3 EXAFS

The ATHENA software²⁸ was used to extract EXAFS oscillations from the raw absorption spectra. Curve fitting with the ARTEMIS software²⁸ was performed in k^3 space. Experimental EXAFS spectra were Fourier-transformed using a Hanning window over the full k range available. Phases and amplitudes for the interatomic scattering paths were calculated with the *ab initio* code FEFF8.40²⁹. Spherical 7.5 Å clusters of atoms built using the fluorite-type structure (space group $Fm\bar{3}m$, i.e. 8 anions at $a\sqrt{3}/4$, 12 cations at $a\sqrt{2}/2$, 24 anions at $a\sqrt{11}/4$ and 6 cations at a) were used for FEFF calculations. For each shell, the coordination numbers were fitted separately. In addition to the three single scattering paths (Me-O, Me-Me and Me-O), one multiple-scattering path (Me-O-Me-O-Me)

was also considered in the FEFF calculations. As often employed for $\text{An}_{\text{LIII}}/\text{LII}$ ^{30–32}, the amplitude factor (S_0^2) was set at 0.90 for U and La shells. The shift in the threshold energy (ΔE_0) was varied as a global parameter.

2.2.4 NMR

All the ¹⁷O NMR experiments were recorded on a 9.4T Bruker spectrometer dedicated for the study of radioactive materials¹⁸. A 4 mm probe was used and the rotor was spun at 15 kHz. The spectra were reference to H₂O (0 ppm) and acquired with a Hahn echo sequence using a 2.5 microsecond pulse for the 90° and synchronized with one rotor period.

3. RESULTS AND DISCUSSION

3.1 FLUORITE AND IDEAL SOLID SOLUTION

The XRD patterns in the Figure 1 show that the three samples exhibit a single fluorite-type phase which is stable at room temperature, as would be expected from the solubility range and thermodynamical calculations^{33–35}. The sharpness of the XRD peaks indicates a good homogeneity of the material.

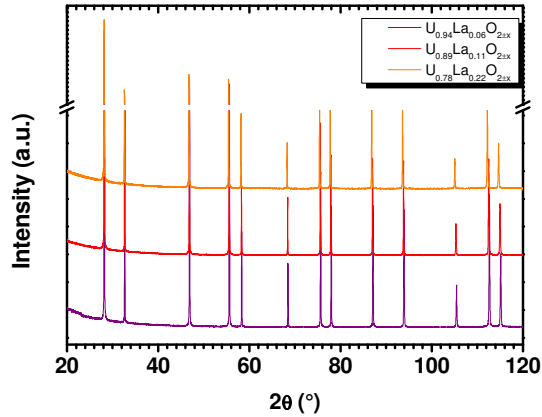


Figure 1: XRD patterns of $\text{U}_{1-y}\text{La}_y\text{O}_{2\pm x}$

The k^3 -weighted EXAFS spectra and their corresponding Fourier transforms (FTs) are presented in the Figure 2. Immediate inspection of the data indicates no difference in the periodicity of the oscillation. A decrease of the EXAFS signals, inversely proportional to the La content, is observed, however.

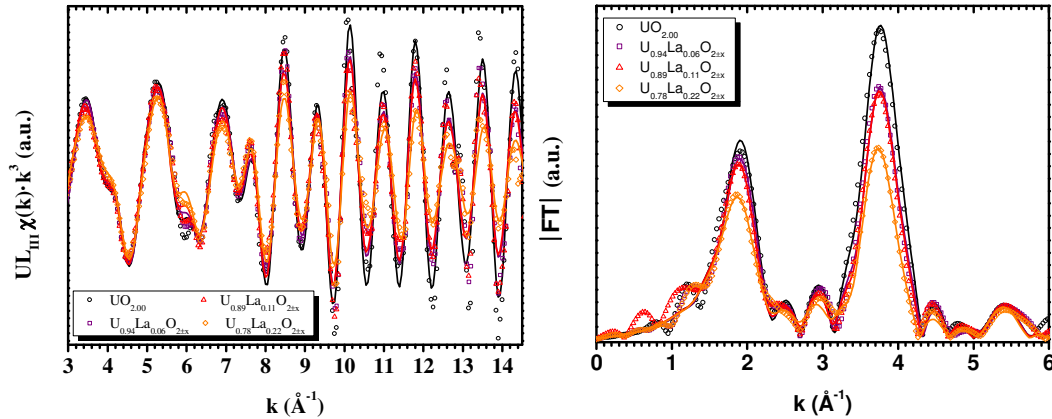


Figure 2: Experimental and fitted U LIII EXAFS spectra of $\text{U}_{1-y}\text{La}_y\text{O}_{2\pm x}$

The good agreement between the experimental and fitted data confirms the validity of the structural model "fluorite solid solution" used in the analysis and described in the section II.2.4. The first coordination shell for each composition is fitted perfectly considering one eight-fold coordinated oxygen shell, discarding then a splitting into sub-shell of the first shell and the presence of O vacancy.

For the $\text{U}_{0.94}\text{La}_{0.06}\text{O}_{2\pm x}$, the first metal shell was fitted with only the U-U distance as a U-La distance cannot be reasonably used in reason of the low La content. For the higher La concentrations, the first metal shell was fitted considering both U-U and U-La distances. One can noticed in Table 2 that the calculated U and La coordination numbers matches quite well those expected from the La content. This supports that the La atoms are randomly distributed in the cation sublattice, i.e. no clustering of La atoms is observed in the structure.

Figure 3 presents the variation of the interatomic distances of $\text{U}_{1-y}\text{La}_y\text{O}_{2\pm x}$ (cf. Table 2) compared to $\text{UO}_{2.00}$. With increasing La content, the first and second U-O distances decrease linearly and both U-U and U-La remains constant. Closely similar behaviours have already been observed in other $\text{U}_{1-y}\text{M}_y\text{O}_{2\pm x}$ ($\text{M}=\text{Am}, \text{Np}$) oxides^{3,4,12}. Likewise, one can notice that the Debye-Waller factor is proportional to the La content, which agrees with an increase of the structural disorder while the doping cation concentration rises.

Table 1: Lattice parameters derived from XRD.

Composition	a (Å)
$\text{U}_{0.94}\text{La}_{0.06}\text{O}_{2\pm x}$	5.4751 (5)
$\text{U}_{0.89}\text{La}_{0.11}\text{O}_{2\pm x}$	5.4798 (5)
$\text{U}_{0.78}\text{La}_{0.22}\text{O}_{2\pm x}$	5.4892 (5)

Table 2: Structural parameters derived from the k^3 -weighted EXAFS spectra (n.c.: not considered in the fit, N_{th} has been calculated from the space group and the chemical composition)

Shell	R (Å)	N	N_{th}	σ^2 (Å ²)
UO_{2.00}				
U-O	2.363 (5)	8.0 (5)	8	0.007 (1)
U-U	3.87 (1)	11.6 (5)	12	0.004 (1)
U-La	n.c.	n.c.		n.c.
U-O	4.53 (1)	24	24	0.008 (1)
U-U	5.47 (1)	6	6	0.007 (1)
U_{0.94}O_{0.06}O_{2±x}				
U-O	2.357 (5)	8.0 (5)	8	0.008 (1)
U-U	3.87 (1)	11.6 (5)2	11.3	0.005 (1)
U-La	n.c.	n.c.	0.7	n.c.
U-O	4.53 (1)	24	24	0.009 (1)
U-U	5.48 (1)	6	6	0.007 (1)
U_{0.89}O_{0.11}O_{2±x}				
U-O	2.348 (5)	8.1 (5)	8	0.008 (1)
U-U	3.87 (1)	10.8 (5)	10.7	0.005 (1)
U-La	3.89 (1)	1.2 (5)	1.3	0.007 (1)
U-O	4.53 (1)	24	24	0.010 (1)
U-U	5.48 (1)	6	6	0.007 (1)
U_{0.78}O_{0.22}O_{2±x}				
U-O	2.338 (5)	8.0 (5)	8	0.011 (1)
U-U	3.87 (1)	9.5 (5)	9.4	0.006 (1)
U-La	3.90 (1)	2.1 (5)	2.6	0.007 (1)
U-O	4.51 (1)	24	24	0.013 (1)
U-U	5.47 (1)	6	6	0.008 (1)

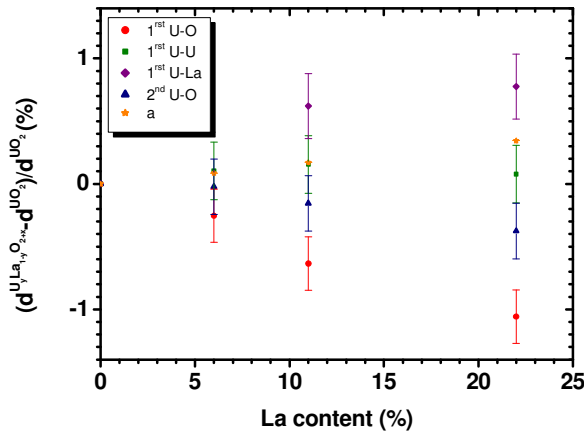


Figure 3: Variation of the interatomic distances and lattice parameters of $U_{1-y}La_yO_{2±x}$ compared to $UO_{2.00}$

3.2 CHARGE DISTRIBUTION

3.2.1 ELECTRONIC ENVIRONMENT

3.2.1.1 La EDGE

The La electronic environment in $U_{1-y}M_yO_{2±x}$ has been studied by La L_{III} HERFD-XANES. Figure 4 presents the La L_{III} HERFD-XANES spectra of the $U_{1-y}La_yO_{2±x}$ ($y=0.06; 0.11; 0.22$) solid solutions and of the $La^{III}O_3$ reference. The $La^{III}O_3$ spectrum shows a single sharp peak at 5491.8 (2) eV. As expected, the maxima of $U_{1-y}La_yO_{2±x}$ white lines are well-aligned with this feature. This result is in perfect agreement with both experimental and theoretical investigations on La-doped systems^{34–36}. In both $La^{III}O_3$ and $U_{1-y}La_yO_{2±x}$, La remains trivalent but their local environments are different, which is illustrated by the different shapes of the spectra white lines. Furthermore, the lack of difference between the 3 (U,La)O₂ HERFD-XANES spectra clearly demonstrated that La cations have the same local environment for the three compositions. In the hexagonal sesquioxide structure (P-3m1)³⁷, La is indeed surrounded by 7 oxygen atoms (3x2.365, 1x2.456 and 3x2.732 Å) whereas La is surrounded by 8 equidistant oxygen atoms in the cubic fluorite structure. To understand the observed difference between La_2O_3 and $U_{1-y}La_yO_{2±x}$, XANES theoretical spectra were calculated using the FDMNES code. The atomic clusters used as input were built using the Fm-3m structure of the UO_2 and by substituting the U central position by one La atom. The difference in ionic radii between U^{IV} (1.00 Å) and La^{III} (1.18 Å) was taken into account with the elongation of the La-O bond length for the first coordination shell; 2.55 Å instead of 2.37 Å. The obtained theoretical spectrum of $U_{0.94}La_{0.06}O_{2±x}$ is shown in Figure 5.

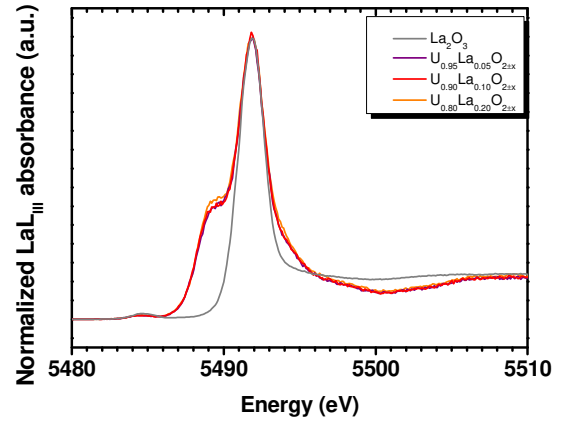


Figure 4: La L_{III} HERFD-XANES spectra of $U_{1-y}La_yO_{2±x}$ with La_2O_3 reference

The white line shape is very well reproduced and allows to conclude that the cubic symmetry around La atoms induced the splitting of the 4d orbital and thus the white line. The projected DOS reveals the electronic states that give rise to the pre-edge and the white line excitation and is plotted in Figure 5. The width of the white line and therefore of the unoccupied d-states reflects the number of O neighbors within the first shell around the La absorber. It must be noted these are preliminary results as the pre-edge at ~ 7 eV below the maximum of the La L_{III} absorption edge observed in both La_2O_3 and experimental spectra is not reproduced in the theoretical spectrum. This pre-edge feature is generally attributed to the mixed dipole and quadrupole

transitions due the presence of an inversion symmetry at the absorbing atom³⁸. Even by taking into account quadrupole contribution during FDMNES calculations, this pre-edge is not present quantitatively. Although this task is beyond the scope of the paper, a mixed dipole quadrupole and dipole can be envisaged and then further calculations considering a distortion of O first shell with different bond lengths should be performed.

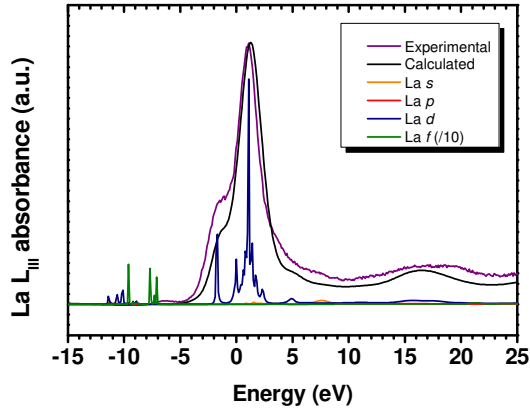


Figure 5: Experimental and calculated U L_{III} XANES spectra of U_{0.94}La_{0.06}O_{2±x}. DOS of La atom absorber

3.2.1.2 U EDGE

The U electronic environment in U_{1-y}La_yO_{2±x} has been studied using U L_{III} XANES which consists into probing the 2p_{3/2}-5d_{5/2} electronic transition. The U L_{III} XANES spectra are presented in Figure 6 with those of the U^{IV}O₂ and (U^{IV}_{0.5}U^V_{0.5})₄O₉ reference. Although within the resolution, the positions of the inflection point and white line, given in Table 3, shows that there is a slight shift of the U_{1-y}La_yO_{2±x} white lines towards higher energies compared to UO₂, suggesting the presence of U^V.

Table 3: Position of the inflection point and the white line of the U M_{IV} and L_{III} XANES spectra.

Composition	La L _{III} edge		U M _{IV} edge		U L _{III} edge	
	WL (eV)	IP (eV)	WL (eV)	IP (eV)	WL (eV)	WL (eV)
U _{0.94} La _{0.06} O _{2±x}	5491.9 (5)	3724.9 (5)	3725.2 (5)	17169.7 (5)	17175.4 (5)	
U _{0.89} La _{0.11} O _{2±x}	5491.8 (5)	3724.9 (5)	3725.3 (5)	17170.3 (5)	17175.5 (5)	
U _{0.78} La _{0.22} O _{2±x}	5491.9 (5)	3724.9 (5)	3725.3 (5)	17170.3 (5)	17176.4 (5)	

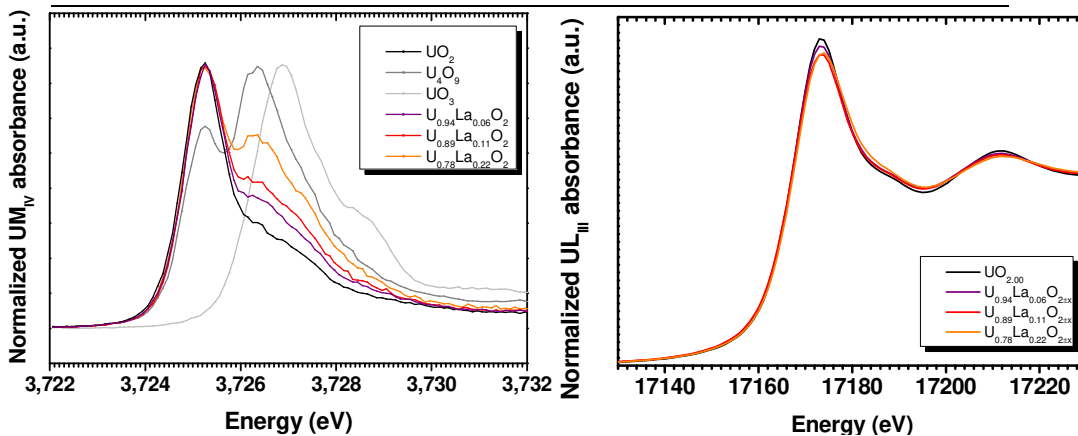


Figure 6: U M_{IV} HERFD-XANES and U L_{III} XANES spectra of U_{1-y}La_yO_{2±x}, UO_{2.00}, U₄O₉ and U₃O₈ references

In the case of U L_{III} XANES, the resolution is limited by the core-hole lifetime of the 2p_{3/2} level (8.2 eV³⁹) and the intrinsic resolution of Si(111) crystal of the monochromator (~2 eV). Applying this method to U M_{IV} edge overcomes core-hole lifetime broadening effects thereby providing spectra with sharper spectral features. Their widths are then no longer limited by the 2p_{3/2} core-hole lifetime but by that of the sharper 3d_{5/2} level in the final state. As an example, the U M_{IV} HERFD-XANES spectra of the U^{IV}O_{2.00}, (U^{IV}_{0.5}U^V_{0.5})₄O₉ and (U^V_{0.67}U^{VI}_{0.33})₃O₈ reference compounds are presented in Figure 6. As previously reported^{21,40-42}, one can see that the U oxidation states are perfectly identifiable at M_{IV} edges. Indeed, the HERFD-XANES spectrum of U^{IV}O_{2.00} shows a sharp peak at 3725.2 (2) eV, due to the transition from the 3d_{5/2} core level to the unoccupied 5f_{5/2} levels. The (U^{IV}_{0.5}U^V_{0.5})₄O₉ HERFD-XANES spectrum presents this same feature characteristic of U^{IV} and also a peak at 3726.2 (2) which in that case correspond to U^V. The (U^V_{0.67}U^{VI}_{0.33})₃O₈ HERFD-XANES spectrum exhibit a white line at 3726.9 (2) eV attributed to U^{VI} and a shoulder at the lower energy side which is at the same position of the (U^{IV}_{0.5}U^V_{0.5})₄O₉ peak characteristic of U^V.

In the U M_{IV} HERFD-XANES spectra of the U_{1-y}La_yO_{2±x} solid solutions, presented in Figure 6, all spectra exhibit the same sharp peak as UO_{2.00}. At the higher energy side of the U_{0.78}La_{0.22}O_{2±x} white line, one can clearly observe a peak which is at the same position as the one characteristic of U^V in (U^{IV}_{0.5}U^V_{0.5})₄O₉, which confirms the presence of U^V. In the case of the samples with lower La content, this peak is comprised between those of UO_{2.00} and U_{0.78}La_{0.22}O_{2±x} and its amplitude decreases with La content. It evidences that U^V was also formed and that its molar fraction is proportional to that of La^{III}. One should mention that we previously have shown with theoretical calculations that the degree of covalency significantly different between UO₂ and these La-doped UO₂⁴¹.

3.2.2 O/M RATIO

3.2.2.1 L_{III} AND M_{IV} XANES

As described in the Experimental section, the U L_{III} XANES spectra have been fitted with a linear combination of the reference samples. The U M_{IV} XANES spectra have been analyzed by IFTA in order to decompose the XANES spectra into the component spectra and the fractions of the components. The factor analysis of these IFTA-extracted component spectra allows a good reproduction of the experimental spectra (cf.

Figure 7).

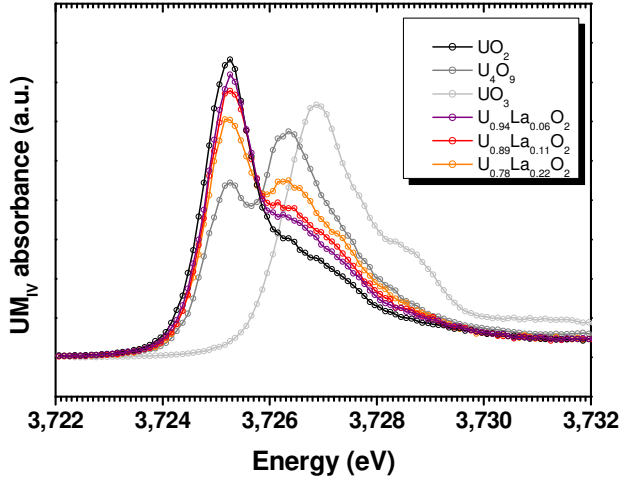


Figure 7: Experimental (—) and fitted (o) U M_{IV} HERFD-XANES derived from IFTA.

The assessed molar fractions are provided in the Table 4. In the case of the IFTA of U M_{IV} XANES spectra, molar fractions of U^{VI} , inferior to 3 (5) % and ranging in the error bar, have been derived. Even if the presence of U^{VI} cannot be formally discarded, it seems however quiet unlikely that U get oxidized to U^{VI} while the U^V molar fractions are inferior to 30%. In addition, one would expect that the U^{VI} molar fractions would increase with the U^V , while in our case the U^{VI} value remains constant. However, the presence of U^{VI} could also be explained by a slight oxidation of the sample surface. Regarding the O/M values, it seems that the obtained values are slightly higher in the case of U M_{IV} XANES than in L_{III} XANES. Although this difference is almost in the uncertainty of both measurements, this deviation is observed systematically for the three studied samples. One can argue that M_{IV} molar fractions are more accurate as they are derived from M_{IV} HERFD-XANES which has an experimental resolution superior to conventional L_{III} XANES. However, this slight discrepancy could also be explained from the difference in the detection methods (i.e. transmission at L_{III}

Table 4: U^{IV} and U^V molar fractions and O/M ratios derived from the linear combination fitting of the U M_{IV} and L_{III} XANES spectra.

Composition	L_{III} edge			M_{IV} edge			
	U^{IV} (%)	U^V (%)	O/M	U^{IV} (%)	U^V (%)	U^{VI} (%)	O/M
$U_{0.94}La_{0.06}O_{2\pm x}$	94 (2)	6 (2)	2.00 (1)	90 (5)	8 (5)	3 (5)	2.03 (1)
$U_{0.89}La_{0.11}O_{2\pm x}$	89 (2)	11 (2)	2.00 (1)	86 (5)	11 (5)	3 (5)	2.02 (1)
$U_{0.78}La_{0.22}O_{2\pm x}$	72 (2)	28 (2)	2.01 (1)	76 (5)	21 (5)	3 (5)	2.01 (1)

and fluorescence at M_{IV}) resulting in a difference of the probed volumes (bulk at L_{III} and surface at M_{IV} (ca. $\sim 0.5 \mu m$)).

3.2.2.2 COMPARISON WITH THE REPORTED EXPERIMENTAL INVESTIGATIONS

In the present work, XANES measurements have shown that stoichiometric oxide solid solutions have been achieved by sintering in Ar/ H_2 at 1923 K. According to our knowledge, O/M ratios equal to 2.00 have been measured in few studies. Indeed, Hill⁴³ has derived the O stoichiometry from the ratio between the U^{IV} content and the total uranium measured by chemical analyses. Stadlbauer *et al.*⁴⁴ have also reported the formation of $U_{1-y}La_yO_{2.00}$ compound for La contents ranging from 0 to 60 at. %. Hinatsu *et al.*⁴⁵ have shown the formation of stoichiometric $U_{0.85}La_{0.15}O_{2.00}$ solid solutions measuring the O/M content in the same heating conditions, Herrero *et al.*⁴⁶ have measured by a back-titration method the formation of a stoichiometric solid solution for a La content of 56 at. %. Although no attempt to measure the O/M ratio has been made, Tsuji *et al.*⁴⁷ have assumed their materials were stoichiometric based on the employed sintering atmosphere. As the O/M ratios of $U_{1-y}M_yO_{2\pm x}$ solid solutions depends on the oxygen partial pressure during the sintering^{4,5,11,48-52}, it cannot be properly determined without experimental measurements. One should mention that the lattice parameters obtained in the present work, are in very good agreement with the reported stoichiometric solid solutions of Hill⁴³, Hinatsu *et al.*⁴⁵, Stadlbauer *et al.*⁴⁴, Herrero *et al.*⁴⁶ and Tsuji *et al.*⁴⁷ (in red on the Figure 8).

Some of the studies on $U_{1-y}La_yO_{2\pm x}$ suggested the formation of hyperstoichiometric materials. Diehl and Keller⁵⁶ have shown that fluorite phases with various stoichiometries can co-exist depending on the sintering conditions. Hund and Peetz⁵⁴ have provided evidence that O/M ratios superior to 2.00 were obtained while heating in air at 1473 K. For a La content ranging between 30 and 52 % at., Herrero *et al.*⁴⁶ have reported similar results for sintering in air at 1673 K. As would have been expected those hyperstoichiometric compounds exhibit lower lattice parameters than the stoichiometric materials (in blue in Figure 8).

Most of the studies on the U-La-O system have reported the formation of hypostoichiometric solid solutions. In opposition with Tsuji *et al.*⁴⁷, Wilson *et al.*⁵⁵ qualified as "reduced" their solid solutions on the basis that the sintering atmosphere was considered as reducing. Hill⁴¹ has also reported O/M ratios inferior to 2 for solid solutions heated in sealed container with metallic uranium chips in vacuum.

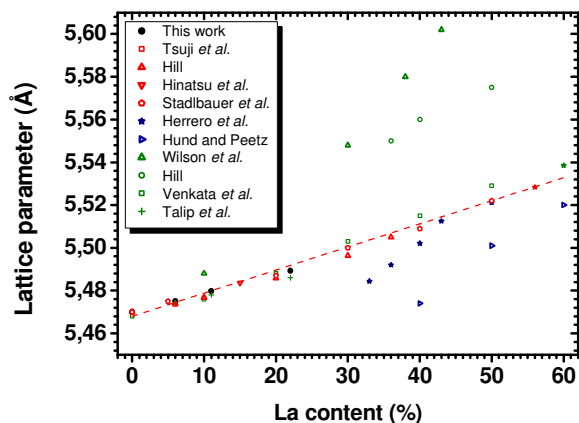


Figure 8: Lattice parameters of $U_{1-y}La_yO_{2\pm x}$ compared with previous works (Tsuji *et al.*⁴⁷: 1273 K / CO/CO₂ mixture ; Hill⁴³: 2023K / Ar-H₂ (Δ); Hinatsu *et al.*⁴⁵; Stadlbauer *et al.*⁴⁴; Venkata *et al.*³⁶: 1873K / Ar-H₂; Talip *et al.*⁵³: 1500 K / Ar-H₂; Herrero *et al.*⁴⁶: 1673K / air; Hund and Peetz⁵⁴: 1473K / air; Wilson *et al.*⁵⁵: 1823K / vacuum; Hill⁴³: 1173K / vacuum with U chip (o); the green, red and blue symbols refer respectively to hypostoichiometric, stoichiometric and hyperstoichiometric solid solutions; the red dashed line is assumed to correspond to the stoichiometric solid solution)

Herrero *et al.*⁴⁶ have shown that hypostoichiometric materials (composed of U^{IV}/U^{VI}) were achieved for $0.56 < y < 0.67$. One should however note the coexistence of U^{IV} and U^{VI} without U^V seems unlikely⁵⁷ even in the hypostoichiometric domain. In those cases, the lattice parameters are significantly higher than those of the stoichiometric materials (in green on the Figure 8). Talip *et al.*⁵³ have assumed hypostoichiometric solid solutions are obtained and affirmed that this supposition is corroborated by the loss of relative intensity of the T_{2g} peaks of the Raman spectra. Venkata-Krishnan *et al.*^{33,36} have shown that the O/M ratios are lower than 2.00 and decrease with increasing La concentration. The O/M ratios were indirectly derived from the concentrations of U^{IV} and U^{VI} which have been determined by measuring the absorbance of these two U cations⁵⁸. Hence, this method relies on the fact that the U charge distribution is not affected by the dissolution of the sintered material in the phosphoric acid. In addition, the possible presence of U^V cannot be considered using this spectrophotometric technique due to its diminution in aqueous solution. Surprisingly, our lattice parameters are in fair agreement with those of Talip *et al.*⁵³ and Venkata-Krishnan *et al.*^{33,36} (green squares and crosses on the Figure 8). However, the reported stoichiometries do not match ours. The lattice parameter being solely affected by the material composition, one expects that similar lattice parameters correspond to close U charge distribution and O stoichiometry. The difference reported here is hardly understandable and may probably come from the difficulty of determining the O/M ratios. This is actually an excellent example illustrating the difficulty of assessing the O/M ratios of $U_{1-y}M_yO_{2\pm x}$ solid solutions without recourse to advanced spectroscopic methods such as XAS.

Despite this discrepancy, Figure 8 shows an overall good agreement between the various studies. Indeed, one can clearly observe two domains: one corresponding to the hypostoichiometric materials (in green) and one defining the hyperstoichiometric compounds (in blue). The reported values for the stoichiometric solid solutions draw a line (in red) which actually

separates quite well the two domains. Lattice parameters significantly bigger than those indicated by this stoichiometric tendency are only achieved in very reducing conditions using metallic uranium. The use of reductive sintering under Ar-H₂ does not seem reductive enough to achieve significant hypostoichiometry, which supports the compensation charge phenomenon described with XANES.

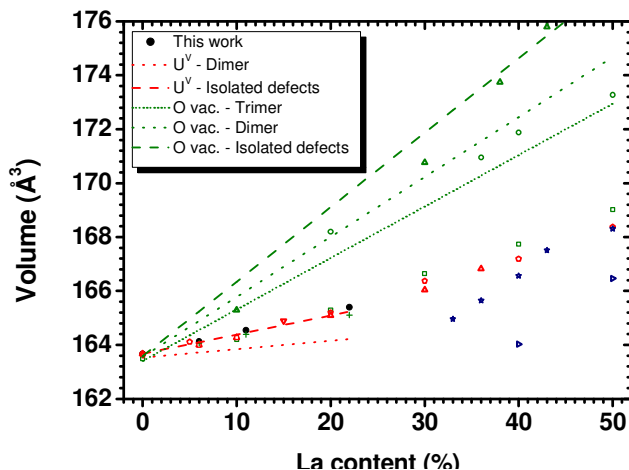


Figure 9: Experimental lattice volume^{43-46,53,53-55,58} of $U_{1-y}La_yO_{2\pm x}$ compared with Mott-Littleton simulations from Desai *et al.*⁵⁹.

3.3 ¹⁷O MAS NMR

The $U_{1-y}La_yO_{2\pm x}$ NMR spectra of the $U_{1-y}La_yO_{2\pm x}$ are presented in Figure 10 and compared to the one of UO_2 . The UO_2 spectrum is characterized by a well-defined single contribution at 713.5 ppm with a full width at half maxima (FWHM) of 1.9 ppm attributed to a single O crystallographic site. The spectrum of $U_{0.94}La_{0.06}O_{2\pm x}$ is already more complex even for such a low La amount. The spectrum is defined by a main peak at 722.3 ppm (value obtained from the position of the gravity centre) with an FWHM of 107.7 ppm and several spinning sidebands are present. This peak is actually the sum of several contributions. In the case of a pure U(IV) compound, three peaks would have been expected: $O(U^{IV})_4$ (78%), $O(U^{IV})_3(La)_1$ (20%) and $O(U^{IV})_2(La)_2$ (2%). However, the present XANES results have shown that U^{IV} and U^V are both present. Therefore, for a randomly distributed network, six peaks are expected with the theoretical relative intensity given in Table 5. The spectrum obtained is accordingly more complicated than for the one expected with only one U oxidation state. One should also not forget the $n=0$ bands which are overlapping with the central transition. For the composition $U_{0.89}La_{0.11}O_{2\pm x}$, eight peaks (Table 5) should theoretically be observed in the NMR spectrum, but again, as a strong overlapping between them exists only one peak at 725.9 ppm with a FWHM of 162.6 ppm can be clearly identified. No strong variation of the center of gravity of the peak is observed compared to the previous spectrum but there is a clear line broadening. The spinning sidebands are still observed contrary to the last spectrum acquired on $U_{0.78}La_{0.22}O_{2\pm x}$ where there is no more resolution even for discriminating the central transition from the spinning sidebands. In this case, thirteen peaks must be present theoretically in the spectrum. These NMR results are quite different from the ones obtained for similar fluorite solid solutions, e.g. La-doped CeO_2 ⁶⁰ or Y-doped

CeO₂⁶¹ for which oxygen vacancies do appear. Indeed, such drastic loss of resolution was not observed and both central transition and spinning sidebands were properly identified. However, a difference lie in that Ce remains tetravalent in presence of La contrary to U. This suggests that the presence of multivalent uranium directly affects the NMR spectra.

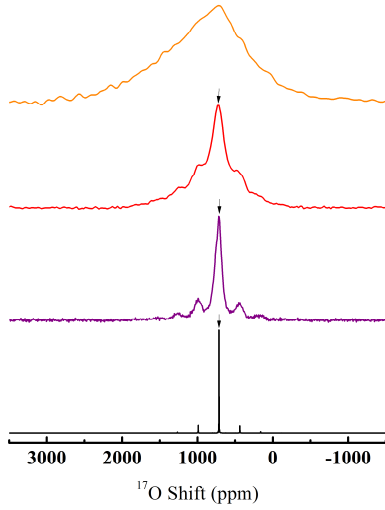


Figure 10: ¹⁷O MAS NMR of UO₂ and U_{1-y}La_yO_{2±x}. The black arrow indicates the peak corresponding to the central transition, the other peaks being the spinning sidebands.

Table 5: Theoretical intensities expected for the O(U^{IV})(U^V)(La) units considering a randomly distributed network.

	Content of La (at.%)		
	x _{La} =6	x _{La} =11	x _{La} =22
O(U ^{IV}) ₄	60	39	10
O(U ^{IV}) ₃ (U ^V) ₁ (La) ₀	16	20	16
O(U ^{IV}) ₃ (U ^V) ₀ (La) ₁	16	22	16
O(U ^{IV}) ₂ (U ^V) ₂ (La) ₀	2	4	9
O(U ^{IV}) ₂ (U ^V) ₀ (La) ₂	2	5	9
O(U ^{IV}) ₂ (U ^V) ₁ (La) ₁	3	8	18
O(U ^{IV}) ₁ (U ^V) ₂ (La) ₁		1	7
O(U ^{IV}) ₁ (U ^V) ₁ (La) ₂		1	7
O(U ^{IV}) ₁ (U ^V) ₀ (La) ₃			2
O(U ^{IV}) ₁ (U ^V) ₀ (La) ₃			2
O(U ^{IV}) ₀ (U ^V) ₃ (La) ₁			1
O(U ^{IV}) ₀ (U ^V) ₂ (La) ₂			2
O(U ^{IV}) ₀ (U ^V) ₁ (La) ₃			1

3.4 FORMATION MECHANISMS OF IDEAL AND STOICHIOMETRIC SOLID SOLUTIONS

The incorporation of non-tetravalent cations in the UO₂ structure is accommodated through the formation of charge compensating defects. In the case of a trivalent cation, such as La^{III}, two mechanisms have been suggested: oxygen vacancy compensation and U^V formation compensation. The first mechanism is

associated with the formation of oxygen vacancies in the hypostoichiometric range. The structure of these solid solutions has been described using a complex defect model implying oxygen vacancies and interstitial atoms^{52,62}. In the second proposed mechanism, the presence of trivalent cation in UO₂ is accommodated *via* the formation of U^V. This mechanism is expected to be dominant in the hyperstoichiometric region. These mechanisms are depending predominantly on the temperature, the oxygen partial pressure and the doping cation content. Considering both above-mentioned mechanisms, thermodynamical modeling^{34,35}, based on the CALPHAD approach⁶³, have been developed to describe the U-La-O ternary system. Contrary to the *ab initio* calculations⁵⁹, it was shown by this approach that the oxygen vacancy formation is almost negligible in deference to U^V formation at an O/M ratio of 2.00.

The accommodation of La^{III} into UO₂ requires then charge compensating defects, i.e. oxygen vacancy and U^V formation, to be formed in the unit cell, leading ultimately to a variation of the lattice volume. Mott-Littleton simulations by Desai *et al.*⁵⁹ predicted an expansion of the lattice volume for both types of defects with increasing La content. However, the volume expansion predicted from the U^V accommodation mechanism is less than that encountered in the case of the formation of oxygen vacancy. For both charge compensating defects, Desai *et al.* have considered several degrees of association of the defects, i.e. isolated defects, dimer defect clusters and trimer defect clusters. Those predictions are compared with our experimental values and those from the literature in Figure 9. One can observe that the predictions involving the formation of oxygen vacancies are matching quite well with the hypostoichiometric domain (in green). Similarly, the volume expansion in the hyperstoichiometric domain (in blue) is predicted fairly well with the dimer configuration of defects in the case of the U^V compensation mechanism. Regarding the data relative to the stoichiometric solid solutions, there is a very good agreement with the predictions using the U^V model around the isolated defect cluster approximation. Then, our data follows the same trend as that predicted in the formation of U^V defects. This is perfectly in agreement with the absence of oxygen vacancy observed in EXAFS and the equimolar fraction of La^{III} and U^V determined by XANES.

4. CONCLUSION

In the UO₂ fluorite structure, the substitution of U^{IV} by aliovalent La^{III} is accommodated by the formation of U^V in quasi equimolar proportion. Despite the cationic substitution, ideal solid solutions are obtained and the fluorite structure is maintained. However, the local structure is slightly affected compared to pure UO₂ with the interatomic distances decreasing with U^V content.

In the literature, it is often assumed, and sometimes admitted without experimental proof, that the incorporation of La^{III} in UO₂ is accommodated through the formation of O vacancies leading then to the formation of hypostoichiometric solid solution. Our result shows that this assumption is wrong and that the O/M ratio cannot be stated without any experimental determination. This statement can be also extended to other U_{1-y}M_yO_{2±x} solid solutions.

AUTHOR INFORMATION

Corresponding Author

* Dr. Damien PRIEUR

d.prieur@hzdr.de

Helmholtz-Zentrum Dresden-Rossendorf, Institute of Resource Ecology, P.O. Box 10119, 01314 Dresden, Germany
Rossendorf beamline (BM20-CRG), European Synchrotron Radiation Facility, 6 rue Jules Horowitz, BP 220, 38043 Grenoble, France

ACKNOWLEDGMENT

The authors acknowledge Co Boshoven, Daniel Bouexière, Sébastien Gardeur, Antony Guiot, Patrick Lajarge, Chris Selfslag, and Sarah Nourry for their help during the sample synthesis and characterization at JRC Karlsruhe. The authors are also grateful to ESRF for providing beamtime.

REFERENCES

- (1) Cordfunke, E. H. P.; Konings, R. J. M. Thermochemical Data for Reactor Materials and Fission Products: The ECN Database. *J. Phase Equilibria* **1993**, *14* (4), 457–464.
- (2) Guéneau, C.; Chartier, A.; Van Brutzel, L. 2.02 - Thermodynamic and Thermophysical Properties of the Actinide Oxides. In *Comprehensive Nuclear Materials*; Konings, R. J. M., Ed.; Elsevier: Oxford, 2012; pp 21–59.
- (3) Prieur, D.; Martin, P.; Lebreton, F.; Delahaye, T.; Banerjee, D.; Scheinost, A. C.; Jankowiak, A. Accommodation of Multivalent Cations in Fluorite-Type Solid Solutions: Case of Am-Bearing UO₂. *J. Nucl. Mater.* **2013**, *434* (1–3), 7–16.
- (4) Prieur, D.; Martin, P. M.; Jankowiak, A.; Gavilan, E.; Scheinost, A. C.; Herlet, N.; Dehaut, P.; Blanchart, P. Local Structure and Charge Distribution in Mixed Uranium-Americium Oxides: Effects of Oxygen Potential and Am Content. *Inorg. Chem.* **2011**, *50* (24), 12437–12445.
- (5) Prieur, D.; Jankowiak, A.; Lechelle, J.; Herlet, N.; Dehaut, P.; Blanchart, P. Reactive Sintering of U_{0.85}Am_{0.15}O_{2-x} Blanket Fuels in Various Oxygen Potentials. *J. Nucl. Mater.* **2012**, *424* (1–3), 285–288.
- (6) McNeilly, C. E.; Chikalla, T. D. Determination of Oxygen/Metal Ratios for Uranium, Plutonium, and (U, Pu) Mixed Oxides. *J. Nucl. Mater.* **1971**, *39* (1), 77–83.
- (7) Prieur, D.; Carvajal-Nunez, U.; Somers, J. O/M Ratio Determination and Oxidation Behaviour of Th_{0.8}Am_{0.2}O_{2-x}. *J. Nucl. Mater.* **2013**, *435* (1–3), 49–51.
- (8) Strach, M.; Belin, R. C.; Richaud, J.-C.; Rogez, J. Influence of Phase Separation on the Oxidation of (U,Pu)O_{2-x}. *J. Phys. Chem. C* **2015**, *119* (40), 23159–23167.
- (9) Schmitz, F.; Dean, G.; Halachmy, M. Application of Lattice Constant Measurements for Stoichiometry Determination in Irradiated U-Pu Mixed Oxide Fuels. *J. Nucl. Mater.* **1971**, *40*, 325–337.
- (10) Ohmichi, T.; Fukushima, S.; Maeda, A.; Watanabe, H. On the Relation between Lattice Parameter and O/M Ratio for Uranium Dioxide-Trivalent Rare Earth Oxide Solid Solution. *J. Nucl. Mater.* **1981**, *102*, 40–46.
- (11) Kato, M.; Konashi, K. Lattice Parameters of (U, Pu, Am, Np)O_{2-x}. *J. Nucl. Mater.* **2009**, *385* (1), 117–121.
- (12) Martin, P.; Grandjean, S.; Valot, C.; Carlot, G.; Ripert, M.; Blanc, P.; Hennig, C. XAS Study of (U_{1-y}Pu_y)O₂ Solid Solutions. *J. Alloys Compd.* **2007**, *444* (Supplement C), 410–414.
- (13) Carvajal-Nunez, U.; Prieur, D.; Vitova, T.; Somers, J. Charge Distribution and Local Structure of Americium-Bearing Thorium Oxide Solid Solutions. *Inorg. Chem.* **2012**, *51* (21), 11762–11768.
- (14) Prieur, D.; Carvajal-Nunez, U.; Vitova, T.; Somers, J. Local and Electronic Structure of Americium-Bearing PuO₂. *Eur. J. Inorg. Chem.* **2013**, No. 9, 1518–1524.
- (15) Boehler, R.; Welland, M. J.; Prieur, D.; Cakir, P.; Vitova, T.; Pruessmann, T.; Pidchenko, I.; Hennig, C.; Guéneau, C.; Konings, R. J. M.; Manara, D. Recent Advances in the Study of the UO₂-PuO₂ Phase Diagram at High Temperatures. *J. Nucl. Mater.* **2014**, *448* (1–3), 330–339.
- (16) Martel, L.; Vigier, J.-F.; Prieur, D.; Nourry, S.; Guiot, A.; Dardenne, K.; Boshoven, J.; Somers, J. Structural Investigation of Uranium-Neptunium Mixed Oxides Using XRD, XANES, and O-17 MAS NMR. *J. Phys. Chem. C* **2014**, *118* (48), 27640–27647.
- (17) Martel, L.; Magnani, N.; Vigier, J.-F.; Boshoven, J.; Selfslag, C.; Farnan, I.; Griveau, J.-C.; Somers, J.; Fanghänel, T. High-Resolution Solid-State Oxygen-17 NMR of Actinide-Bearing Compounds: An Insight into the 5f Chemistry. *Inorg. Chem.* **2014**, *53* (13), 6928–6933.
- (18) Martel, L.; Somers, J.; Berkmann, C.; Koepp, F.; Rothermel, A.; Pauvert, O.; Selfslag, C.; Farnan, I. A Nuclear Magnetic Resonance Spectrometer Concept for Hermetically Sealed Magic Angle Spinning Investigations on Highly Toxic, Radiotoxic, or Air Sensitive Materials. *Rev. Sci. Instrum.* **2013**, *84* (5), 055112.
- (19) Bastow, T. J. 139La Nuclear Magnetic Resonance Characterisation of La₂O₃ and La_{1-x}Sr_xMO₃ Where M = Cr, Mn or Co. *Solid State Nucl. Magn. Reson.* **1994**, *3* (1), 17–22.
- (20) Matz, W.; Schell, N.; Bernhard, G.; Prokert, F.; Reich, T.; Claußner, J.; Oehme, W.; Schlenk, R.; Dienel, S.; Funke, H.; Eichhorn, F.; Betzl, M.; Pröhl, D.; Strauch, U.; Hüttig, G.; Krug, H.; Neumann, W.; Brendler, V.; Reichel, P.; Denecke, M. A.; Nitsche, H. ROBL – a CRG Beamline for Radiochemistry and Materials Research at the ESRF. *J. Synchrotron Radiat.* **1999**, *6* (6), 1076–1085.
- (21) Kvashnina, K. O.; Butorin, S. M.; Martin, P.; Glatzel, P. Chemical State of Complex Uranium Oxides. *Phys. Rev. Lett.* **2013**, *111* (25), 253002.
- (22) Glatzel, P.; Bergmann, U. High Resolution 1s Core Hole X-Ray Spectroscopy in 3d Transition Metal Complexes—electronic and Structural Information. *Coord. Chem. Rev.* **2005**, *249* (1), 65–95.
- (23) Kvashnina, K. O.; de Groot, F. M. F. Invisible Structures in the X-Ray Absorption Spectra of Actinides. *J. Electron Spectrosc. Relat. Phenom.* **2014**, *194*, 88–93.
- (24) Kvashnina, K. O.; Kvashnin, Y. O.; Butorin, S. M. Role of Resonant Inelastic X-Ray Scattering in High-Resolution Core-Level Spectroscopy of Actinide Materials. *J. Electron Spectrosc. Relat. Phenom.* **2014**, *194*, 27–36.
- (25) Leinders, G.; Bes, R.; Pakarinen, J.; Kvashnina, K.; Verwerft, M. Evolution of the Uranium Chemical State in Mixed-Valence Oxides. *Inorg. Chem.* **2017**, *56* (12), 6784–6787.
- (26) Roßberg, A.; Reich, T.; Bernhard, G. Complexation of Uranium(VI) with Protocatechuic Acid—application of Iterative Transformation Factor Analysis to EXAFS Spectroscopy. *Anal. Bioanal. Chem.* **2003**, *376* (5), 631–638.
- (27) Bunău, O.; Joly, Y. Self-Consistent Aspects of x-Ray Absorption Calculations. *J. Phys. Condens. Matter* **2009**, *21* (34), 345501.
- (28) Ravel, B.; Newville, M. ATHENA, ARTEMIS, HEPHAESTUS: Data Analysis for X-Ray Absorption Spectroscopy Using IFEFFIT. *J. Synchrotron Radiat.* **2005**, *12* (4), 537–541.
- (29) Rehr, J. J.; Kas, J. J.; Vila, F. D.; Prange, M. P.; Jorissen, K. Parameter-Free Calculations of X-Ray Spectra with FEFF9. *Phys. Chem. Chem. Phys.* **2010**, *12* (21), 5503–5513.
- (30) Prieur, D.; Lebreton, F.; Caisso, M.; Martin, P. M.; Scheinost, A. C.; Delahaye, T.; Manara, D. Melting Behaviour of Americium-Doped Uranium Dioxide. *J. Chem. Thermodyn.* **2016**, *97*, 251–259.
- (31) Prieur, D.; Vigier, J.-F.; Rothe, J.; Somers, J. Comparison of XRD, XANES and TGA Methods to Assess the O/M Ratio of Th_{0.60}Am_{0.40}O_{2-x}. *J. Nucl. Mater.* **2014**, *448* (1–3), 4–7.
- (32) Tyrpekl, V.; Naji, M.; Holzhäuser, M.; Freis, D.; Prieur, D.; Martin, P.; Cremer, B.; Murray-Farthing, M.; Cologna, M. On the Role of the Electrical Field in Spark Plasma Sintering of UO_{2+x}. **2017**, *7*, 46625.
- (33) Venkata Krishnan, R.; Panneerselvam, G.; Antony, M. P.; Nagarajan, K. Solubility Studies and Thermal Expansion Coefficient of Uranium-lanthanum Mixed Oxide System. *J. Nucl. Mater.* **2010**, *403* (1), 25–31.
- (34) McMurray, J. W.; Shin, D.; Besmann, T. M. Thermodynamic Assessment of the U₂La₂O₇ System. *J. Nucl. Mater.* **2015**, *456*, 142–150.

- (35) Shin, D.; Besmann, T. M. Thermodynamic Modeling of the (U,Ln)O_{2±x} Solid Solution Phase. *J. Nucl. Mater.* **2013**, *433* (1), 227–232.
- (36) Venkata Krishnan, R.; Mittal, V. K.; Babu, R.; Senapati, A.; Bera, S.; Nagarajan, K. Heat Capacity Measurements and XPS Studies on Uranium-Lanthanum Mixed Oxides. *J. Alloys Compd.* **2011**, *509* (7), 3229–3237.
- (37) Aldebert, P.; Traverse, J. P. Etude Par Diffraction Neutronique Des Structures de Haute Temperature de La₂O₃ et Nd₂O₃. *Mater. Res. Bull.* **1979**, *14* (3), 303–323.
- (38) Hirsch, O.; Kvashnina, K.; Willa, C.; Koziej, D. Hard X-Ray Photon-in Photon-out Spectroscopy as a Probe of the Temperature-Induced Delocalization of Electrons in Nanoscale Semiconductors. *Chem. Mater.* **2017**, *29* (4), 1461–1466.
- (39) Campbell, J. L.; Papp, T. Widths of the Atomic K-N7 Levels. *At. Data Nucl. Data Tables* **2001**, *77* (1), 1–56.
- (40) Vitova, T.; Denecke, M. A.; Goettlicher, J.; Jorissen, K.; Kas, J. J.; Kvashnina, K.; Pruessmann, T.; Rehr, J. J.; Rothe, J. Actinide and Lanthanide Speciation with High-Energy Resolution X-Ray Techniques. In *15th International Conference on X-Ray Absorption Fine Structure (xafs15)*; Wu, Z. Y., Ed.; Iop Publishing Ltd: Bristol, 2013; Vol. 430, p UNSP 012117.
- (41) Butorin, S. M.; Kvashnina, K. O.; Prieur, D.; Rivenet, M.; Martin, P. M. Characteristics of Chemical Bonding of Pentavalent Uranium in La-Doped UO₂. *Chem. Commun.* **2017**, *53* (1), 115–118.
- (42) Butorin, S. M.; Kvashnina, K. O.; Smith, A. L.; Popa, K.; Martin, P. M. Crystal-Field and Covalency Effects in Uranates: An X-Ray Spectroscopic Study. *Chem. – Eur. J.* **2016**, *22* (28), 9693–9698.
- (43) Hill, D. C. Phase Relations and Crystal Chemistry in the System Uranium Oxide–Lanthanum Oxide. *J. Am. Ceram. Soc.* **1962**, *45* (6), 258–263.
- (44) Stadlbauer, E.; Wichmann, U.; Lott, U.; Keller, C. Thermodynamics and Phase Relationships of the Ternary Lanthanum-Uranium-Oxygen System. *J. Solid State Chem.* **1974**, *10* (4), 341–350.
- (45) Hinatsu, Y. Magnetic Studies on (U, Ln)O_{2+x} Solid Solutions: II. Magnetic Susceptibilities of Solid Solutions with High Lanthanum and Oxygen Concentrations. *J. Solid State Chem.* **1991**, *95* (2), 300–306.
- (46) Herrero, P.; Rojas, R. M.; García, P. The U□Ca□La□O and U□La□O Systems: A Comparative Study. *Inorganica Chim. Acta* **1987**, *140* (Supplement C), 159–160.
- (47) Tsuji, T.; Iwashita, M.; Yamashita, T.; Ohuchi, K. Effect of Cations on Lattice Constants of (MyU_{1-y})O_{2.00} (M=Pu, Th, La) at Low Doped Cation Concentrations. *J. Alloys Compd.* **1998**, *271* (Supplement C), 391–394.
- (48) Kato, M.; Tamura, T.; Konashi, K. Oxygen Potentials of Mixed Oxide Fuels for Fast Reactors. *J. Nucl. Mater.* **2009**, *385*, 419–423.
- (49) Kato, M.; Konashi, K.; Nakae, N. Analysis of Oxygen Potential of (U_{0.7}Pu_{0.3})O_{2±x} and (U_{0.8}Pu_{0.2})O_{2±x} Based on Point Defect Chemistry. *J. Nucl. Mater.* **2009**, *389* (1), 164–169.
- (50) Kim, H. S.; Yoon, Y. K.; Lee, Y. W. Defect Structures of U_{1-y}Er_yO_{2±x} Solid Solutions. *J. Nucl. Mater.* **1995**, *226*, 206–215.
- (51) Osaka, M.; Kurosaki, K.; Yamanaka, S. Oxygen Potential of (Pu_{0.91}Am_{0.09})O_{2-x}. *J. Nucl. Mater.* **2006**, *357* (1), 69–76.
- (52) Yoshida, K.; Arima, T.; Inagaki, Y.; Idemitsu, K.; Osaka, M.; Miwa, S. Oxygen Potential of Hypo-Stoichiometric La-Doped UO₂. *J. Nucl. Mater.* **2011**, *418* (1), 22–26.
- (53) Talip, Z.; Wiss, T.; Raison, P. E.; Paillier, J.; Manara, D.; Somers, J.; Konings, R. J. M. Raman and X-Ray Studies of Uranium–Lanthanum-Mixed Oxides Before and After Air Oxidation. *J. Am. Ceram. Soc.* **2015**, *98* (7), 2278–2285.
- (54) Hund, F.; Peetz, U. Über Weitere Fluoritphasen in Den Mischoxyden Seltener Erden Mit Uran - Untersuchungen Der Systeme La₂O₃, Nd₂O₃, Sm₂O₃, Yb₂O₃, Sc₂O₃ Mit U₃O₈. *Z. Anorg. Allg. Chem.* **1952**, *271* (1–2), 6–16.
- (55) Wilson, W. B. Stabilisation of UO₂ by Valence Compensation. *USAEC report* **1959**, *BMMI-1318*.
- (56) Diehl, H. G.; Keller, C. Das System UO₂□UO₃□LaO_{1.5}. *J. Solid State Chem.* **1971**, *3* (4), 621–636.
- (57) Guéneau, C.; Baichi, M.; Labroche, D.; Chatillon, C.; Sundman, B. Thermodynamic Assessment of the Uranium–oxygen System. *J. Nucl. Mater.* **2002**, *304* (2), 161–175.
- (58) Krishnan, R. V.; Panneerselvam, G.; Manikandan, P.; Antony, M. P.; Nagarajan, K. Heat Capacity and Thermal Expansion of Uranium-Gadolinium Mixed Oxides. *J. Nucl. Radiochem. Sci.* **2009**, *10* (1), 1_19-1_26.
- (59) Desai, K. Atomic-scale simulation of soluble fission products in UO₂. <https://publications.europa.eu/en/publication-detail/-/publication/a565d9ef-e7b9-4148-ad1e-640862e6d5dd/language-en> (accessed Sep 29, 2017).
- (60) Heinmaa, I.; Joon, T.; Kooskora, H.; Pahapill, J.; Subbi, J. Local Structure and Oxygen Ion Dynamics in La Doped Ceria: 17O NMR Study. *Solid State Ion.* **2010**, *181* (29), 1309–1315.
- (61) Kim, N.; Stebbins, J. F. Vacancy and Cation Distribution in Yttria-Doped Ceria: An 89Y and 17O MAS NMR Study. *Chem. Mater.* **2007**, *19* (23), 5742–5747.
- (62) Matsui, T.; Naito, K. Electrical Conductivity Measurement and Thermogravimetric Study of Lanthanum-Doped Uranium Dioxide. *J. Nucl. Mater.* **1986**, *138*, 19–26.
- (63) *CALPHAD*, 1 edition.; Saunders, N., Miodownik, A. P., Eds.; Pergamon: Oxford, 1998.

SYNOPSIS TOC.

